TiO$_2$-SiO$_2$ Nanocomposite Saturable Absorber for Ultrafast Photonics

Norita Mohd Yusoff, *Member, IEEE*, Eng Khoon Ng, Natrah Shafiqah Rosli, Che Azurahanim Che Abdullah, Nelydia Md. Yusoff ⓘ, *Senior Member, IEEE*, and Mohd Adzir Mahdi ⓘ, *Senior Member, IEEE*

Abstract—A tapered microfiber decorated with titanium dioxide-silicon dioxide nanocomposite saturable absorber (TiO$_2$-SiO$_2$-SA) is demonstrated via alkali fusion method and spin-coating technique. The TiO$_2$-SiO$_2$-SA exhibited 17.1% modulation depth, 31.7 μJ/cm^2 saturation fluence and 35.4% non-saturable loss. The TiO$_2$-SiO$_2$-SA was able to generate a pulse duration of 797 fs at a repetition rate of 10.39 MHz and an average output power of 16.57 mW at 1.56 μm. This work presents an enhanced pulse duration within titanium-based saturable absorbers. The high damage threshold of beyond 24.82 GW/cm^2 and excellent stability are believed to have opened a new route of using nanomaterials derived from waste product for next generation ultrafast photonic applications.

Index Terms—Erbium-doped fiber laser, mode-locked, saturable absorber, silicon dioxide, titanium dioxide.

I. INTRODUCTION

PULSE fiber lasers based on material integrated saturable absorbers (SA) have recently garnered a huge research interest in photonics communities. Over the past decades, the considerable success of SAs employing graphene [1] and other two-dimensional materials [2], [3] has triggered the emergence of metal nanoparticles [4], [5], metal oxides [6], and transition metal oxides [7], [8], [9] for ultrafast photonics. Titanium dioxide (TiO$_2$) is a transition metal oxide with crystal structures of anatase, rutile and brookite. TiO$_2$ has been vigorously applied in many fields in photonics due to its outstanding nonlinear optical properties [10], [11]. In addition, the high nonlinear refractive index of TiO$_2$ promotes strong light confinement in optical

Norita Mohd Yusoff is with the Wireless and Photonics Networks Research Centre, Faculty of Engineering, Universiti Putra Malaysia, 43400 Serdang, Selangor, Malaysia (e-mail: gs58032@student.upm.edu.my).

Eng Khoon Ng is with the Department of Engineering, University of Cambridge, Cambridge CB3 0FA, U.K. (e-mail: khoon_cloud@hotmail.com).

Natrah Shafiqah Rosli and Che Azurahanim Che Abdullah are with the Institute of Nanoscience and Nanotechnology (ION2) and Department of Physics, Faculty of Science, Universiti Putra Malaysia, 43400 Serdang, Selangor, Malaysia (e-mail: natrah_sha@yahoo.com; azurahanim@upm.edu.my).

Nelydia Md. Yusoff is with the Razak Faculty of Technology and Informatics, Universiti Teknologi Malaysia Kuala Lumpur, 54100 Kuala Lumpur, Malaysia (e-mail: nelidya.kl@utm.my).

Mohd Adzir Mahdi is with the Wireless and Photonics Networks Research Centre, Faculty of Engineering, Universiti Putra Malaysia, 43400 Serdang, Selangor, Malaysia (e-mail: mam@upm.edu.my).

Digital Object Identifier 10.1109/JPHOT.2023.3237513

waveguides [12], [13]. Furthermore, the strong nonlinearity of TiO$_2$ is beneficial for supercontinuum generation [14]. Besides that, the transparency window of TiO$_2$ from ultraviolet towards near-infrared bands make it a fascinating candidate for various applications like photocatalysis [15], solar cells [16] and pulse fiber laser technology [17], [18], [19], [20]. Previous works reported that TiO$_2$ had large modulation depth up to 34% [20] and two-photon absorption-free in near-infrared region [14], which allows it to maintain the fundamental mode-locking over wide pump power ranges [17]. Despite the successful attempts of TiO$_2$ as light absorbing material for pulse generation [17], [18], [19], [20], the achieved pulse durations within micro- to pico-seconds are still lagged behind other existing materials [21], [22], [23]. Currently, numerous initiatives have been made to produce nanoparticles from waste resources for sensor, actuator, and supercapacitor applications [24]. The synthesis of nanoparticles in a greener way lowers the overall cost as well as uses fewer hazardous chemicals as compared to the well-established routes such as sol-gel, hydrothermal, solvothermal, surfactant-assisted, micro-emulsion and templated method [25].

In the past years, silicon dioxide (SiO$_2$) had gained significant interest due to its high tolerance to extreme conditions like acidity and basicity, high temperature, and humid environment [26], [27]. In addition, it has been widely used as a coating layer for metal oxides [28], [29]. Furthermore, it has been reported that the introduction of SiO$_2$ layer is capable to inhibit the aggregation of nanomaterials [30]. In fact, Li et al. stated that the incorporation of SiO$_2$ does not contribute to the additional scattering effect as its refractive index matched with silica optical fiber [31]. Moreover, the sol-gel approach of material-SiO$_2$ has been proven to boost the damage threshold of the SA device as it helps to dissipate heat and isolates the material from chemical degradation [32], [33]. For instance, a high damage threshold of graphene-SA [34] and molybdenum disulfide (MoS$_2$)-SA [31] up to 50.7 GW/cm^2 and 3.46 J/cm^2, respectively have been recorded after SiO$_2$ incorporation. In other work, Lv and associates reported superior stability of MoS$_2$/SiO$_2$-SA under 600 mW pump power over one week monitoring period [33].

Therefore, motivated by these merits, we demonstrate an ultrafast 797 fs pulse duration of mode-locked erbium-doped fiber laser (ML-EDFL) via TiO$_2$-SiO$_2$ decorated onto a tapered microfiber (TMF) with the help of polydimethylsiloxane (PDMS) polymer matrix. The delivered pulse performance is significantly improved as compared to the previously reported titanium-based SAs. The findings show that the TiO$_2$-SiO$_2$-SA

exhibited modulation depth and saturation fluence of 17.10% and 31.7 μJ/cm^2, respectively. The estimated damage threshold of this SA exceeded 24.82 GW/cm^2 input intensity, which was determined from the back-calculation method based on the laser output power. The reutilization of industrial ilmenite waste as a precursor for nanomaterial production paves an ecofriendly route for waste minimization and extends the exploration of composite materials for ultrafast photonics.

II. MATERIALS, METHODS AND CHARACTERIZATIONS

A. Chemicals

Synthetic rutile made from ilmenite waste was procured from a tin mining factory in Perak, Malaysia. Sodium hydroxide (NaOH) was obtained from R&M Chemical while sulfuric acid (H$_2$SO$_4$) was purchased from Emsure. The isopropyl alcohol (IPA, 99.5%), ethanol (99.5%) and silica (SiO$_2$) nanoparticles were ordered from Sigma Aldrich, and PDMS prepolymer and curing agent (Sylgard184) was acquired from Dow Corning. In this work, all the chemicals were utilized as received without further purification.

B. Material Synthesis and Characterizations

TiO$_2$ nanoparticles were synthesized using the optimized procedures of alkali fusion method [35]. Initially, bulk synthetic rutile and NaOH were mixed at the mass ratio of 1:2, followed by calcination at 550 °C for 3 hours. The product then went through a leaching process by introducing 2 M of H$_2$SO$_4$ under continuous stirring condition at 80 °C for another 3 hours. This step is crucial to maximize the interaction between the product and strong acid [36]. Finally, the resultant product was washed a few times using deionized water and dried at 80 °C for 24 hours. The product was subsequently crushed using mortar and pestle to obtain powders with reduced particle sizes. Next, to prepare TiO$_2$-SiO$_2$ nanocomposite, the aggregated raw SiO$_2$ was firstly dispersed in ethanol, ball-milled for 90 minutes with the help of ceramic grinding ball. After that, the product was collected after ball separation, filtration, and desiccation. Following that, the SiO$_2$ powders was dissolved in NaOH solution at 60 °C under stirring condition. It was then mixed with aged TiO$_2$ with a mass ratio of 1:1 and subsequently stirred for 1.5 hours. By calcinating the sample at 300 °C for several hours, the final product of TiO$_2$-SiO$_2$ nanocomposite was produced.

The phase identification of as-synthesized TiO$_2$-SiO$_2$ was characterized using Rigaku SmartLab X-ray diffractometer (XRD) equipped with Cu-Kα radiation of wavelength, λ = 0.15406 nm. The measurement was taken within the 2θ range of 20° to 80° with an interval of 0.02°. Fig. 1 shows the XRD pattern with peaks at 25.23° (101), 37.79° (004), 47.88° (200), 54.85° (105), 62.55° (204) and 74.89° (215) which can be indexed as anatase phase of TiO$_2$ [35], [37] and matched well with the reference code (JCPDS 96-900-8214). Meanwhile, the visible peaks at 27.38° (110), 36.02° (101) and 69.69° (112) represent the rutile phase of TiO$_2$ (JCPDS 96-900-9084) [38]. Both phases crystallized in tetragonal systems; the lattice parameters of anatase and rutile are a = b = 3.78 Å, c = 9.51 Å, and
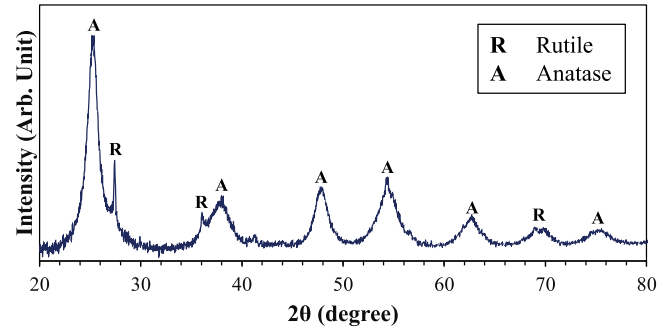

Fig. 1. Diffractogram of the as-synthesized TiO$_2$-SiO$_2$.

a = b = 4.60 Å, c = 2.96 Å, respectively. From the XRD analysis, the percentage of anatase and rutile TiO$_2$ are 90.4% and 9.6%, respectively. The broadening of the XRD peaks reveals the reduced crystallite size after the leaching process. The average crystallite size (D) of anatase TiO$_2$ is then estimated using the Scherrer equation in (1) as follows:

$$D = \frac{0.9\lambda}{\beta \cos\theta} \qquad (1)$$

where β is the full width at half maximum (FWHM) of the most intense XRD peak and θ is the Bragg's angle. As a result, the value of D at $2\theta = 25.23°$ is 6.12 nm. Conversely, representative of SiO$_2$ was not observed as a consequence of their non-crystalline phase (amorphous) in nature.

The sample was subjected to transmission electron microscopy (TEM) via Hitachi H-7100 STEM coupled with energy dispersive X-ray (EDX). Fig. 2(a) shows nanosheet-like morphology of TiO$_2$-SiO$_2$. The magnified TEM image in Fig. 2(b) reveals the successful coating of crystalline TiO$_2$ with amorphous SiO$_2$. Specifically at point 1 (refer Fig. 2(c)), the weight percentage of titanium (Ti), oxygen (O), and silicon (Si) are 57.6%, 30.6%, and 6.60%, respectively. Meanwhile, the lowest percentage of Ti (5.10%) is represented by point 2 (refer Fig. 2(d)), as compared to O (28.90%) and Si (31.30%). The detected sulphur (S) in the EDX analysis is associated with the incomplete removal of acid during the leaching process. Meanwhile, the identified carbon (C) element is due to the slight burnt of the sample caused by intense electron beam during TEM characterization. Fig. 3(a), (b) present the absorption profile of TiO$_2$-SiO$_2$ spanning from ultra-violet towards near-infrared region. From Fig. 3(a), the absorption edge was estimated to be 405 nm, which matched with the previously reported work in [39]. By considering the absorption edge wavelength (λ), Planck's constant (h), and velocity of light (c) expressed in (2) below;

$$E_g = \frac{hc}{\lambda}, \qquad (2)$$

the optical bandgap energy (E_g) of TiO$_2$-SiO$_2$ was estimated to be 3.06 eV [39]. The E_g and particle size share an inverse correlation to each other, in which an absorption edge shifts to a shorter wavelength with reducing particle size [40]. This finding is supported by XRD analysis whereby broad β was obtained as depicted in Fig. 1, implying the size of the
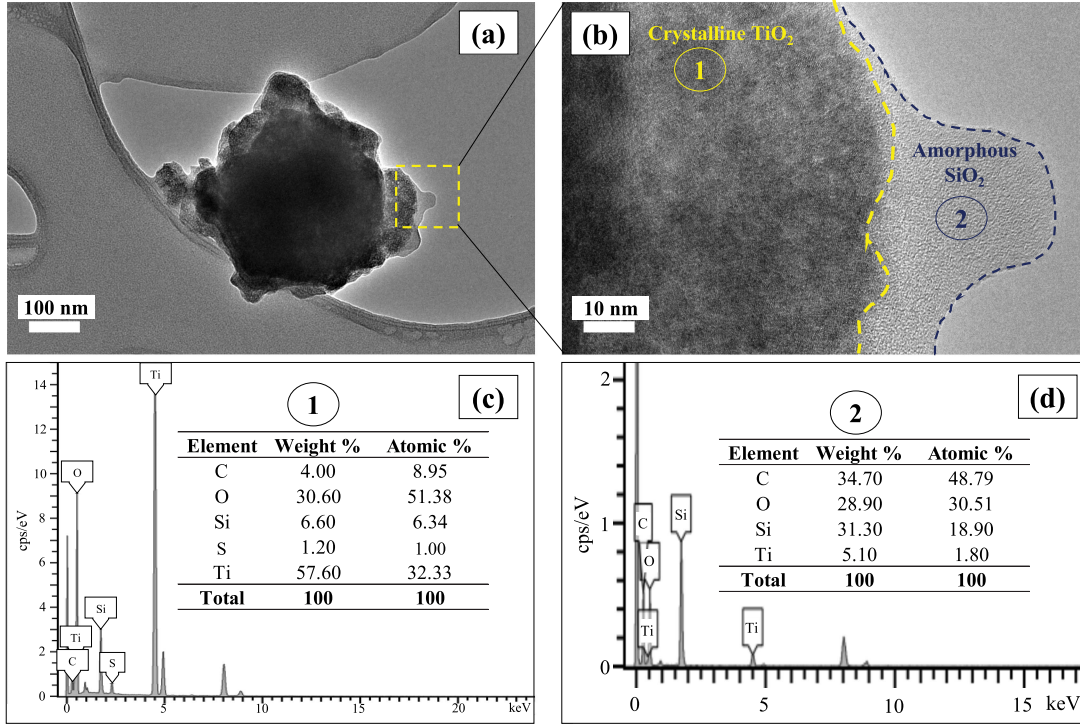
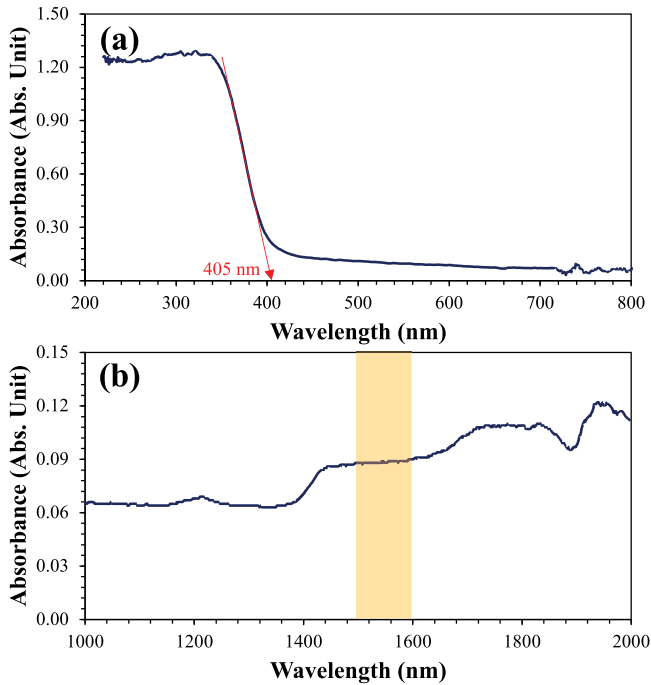Fig. 2. (a), (b) TEM images and (c), (d) EDX analysis of the as-synthesized TiO$_2$-SiO$_2$.

Fig. 3. (a) Ultraviolet-visible and (b) near-infrared absorption profile of as-synthesized TiO$_2$-SiO$_2$.

synthesized TiO$_2$-SiO$_2$ lies within the nanometer regime. Apart from that, a defect-free semiconducting material only allows incident photons with energy equal to the E_g to be absorbed [41]. However, the non-negligible absorption of TiO$_2$-SiO$_2$ across 1000–2000 nm observed in Fig. 3(b) is due to the crystal

imperfections (such as vacancies, atom dislocations, etc.) that extends the material's absorption bands [41]. The consistent absorption profile in 1500–1600 nm wavelength (refer shaded region in Fig. 3(b)) proved its functionality as light absorbing material for our ML-EDFL laser system.

C. TiO$_2$-SiO$_2$-SA Fabrication and Characterizations

As schematically sketched in Fig. 4(a), TiO$_2$-SiO$_2$-PDMS nanocomposite was prepared by firstly dispersing 0.5 mg of TiO$_2$-SiO$_2$ nanoparticles in 10 mL of IPA. Thereafter, the glass vial was then filled with 1 g of PDMS and the mixture was heated to 85 °C and agitated magnetically for 24 hours. Next, 0.1 g of curing agent was introduced to the TiO$_2$-SiO$_2$-PDMS nanocomposite, followed by constant magnetic stirring for 30 minutes to retain its homogeneity. The air bubbles were then removed from the nanocomposite through a degassing process in vacuum. The TMF properties were set at 30 mm (taper transition), 0.5 mm (waist length) and 10 μm (waist diameter), as shown in Fig. 4(b). The adiabaticity of the TMF was firstly determined prior to its fabrication by calculating the taper angle, θ, using the following expression [42];

$$\tan \theta = \frac{D_1 - D_2}{2L} \qquad (3)$$

where D$_1$ is the cladding diameter, D$_2$ is the waist diameter, and L is the taper transition length. The calculated value of θ was 1.92 mrad which was less than 5 mrad, validating its adiabatic criterion [42]. In addition, the adiabaticity can also be confirmed from its features of having low loss and no obvious spectral fringes [42]. Next, the acrylate polymer coating layer of single-mode fiber was stripped off and the unstripped optical
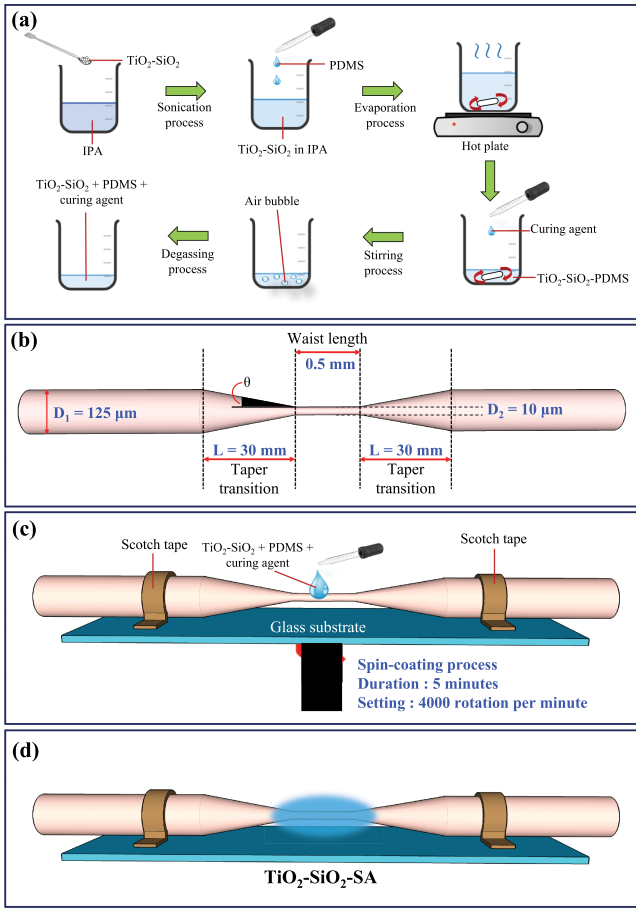
Fig. 4. (a) The preparation of TiO_2-SiO_2-PDMS nanocomposite, (b) illustration of the fabricated TMF, (c) spin-coating process, and (d) TiO_2-SiO_2-PDMS nanocomposite deposited TMF.
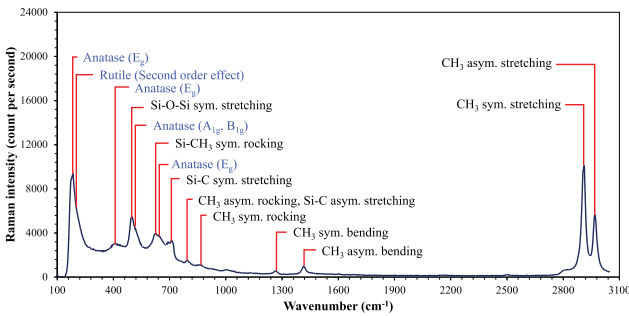

Fig. 5. Raman spectrum of cured TiO_2-SiO_2-PDMS nanocomposite.

fiber were locked on the stage holder of Vytran GPX-3400 optical glass processing workstation for precise TMF fabrication. As depicted in Fig. 4(c), the final as-prepared TiO_2-SiO_2-PDMS nanocomposite with curing agent was spin-coated at the rotating speed of 4000 rotation per minute for 5 minutes. Lastly, the as-fabricated TiO_2-SiO_2-SA was left to dry (refer Fig. 4(d)).

The remaining cured TiO_2-SiO_2-PDMS nanocomposite in the glass vial was analyzed using Raman spectroscopy (Horiba Scientific-LabRAM HR Evolution, 532 nm excitation wavelength). As shown in Fig. 5, the active Raman modes of anatase

TiO_2 were detected at 144 cm^{-1} (E_g), 399 cm^{-1} (B_{1g}), 514 cm^{-1} (A_{1g}, B_{1g}) and 639 cm^{-1} (E_g) whereas second order Raman of rutile phase was identified at 240 cm^{-1} [43]. On the other hand, the well-resolved Raman peaks of PDMS at 2908 cm^{-1} and 2967 cm^{-1} as well as other minor peaks that overlapped with SiO_2 (refer Fig. 5) signify the successful preparation of the nanocomposite [44].

The characteristics of bare TMF and TiO_2-SiO_2-SA were investigated in terms of their linear transmission properties. This property was characterized using Amonics ALS-CL-17-B-SC broadband light source and Yokogawa optical spectrum analyzer model AQ6370B with a resolution of 0.02 nm, as depicted in Fig. 6(a). The bare TMF was spliced in between these instruments followed by TiO_2-SiO_2-SA. The transmission profiles of both samples are plotted in Fig. 6(b). In the case of un-tapered region, the light propagation obeys the total internal reflection. The tapering process causes the light to propagate outside the fiber core/cladding as evanescent waves. Unlike lossy feature of non-adiabatic TMF with obvious fringes on the transmitted spectrum, the experimental finding in Fig. 6(b) shows the transmission of beyond 95% with no distinct fringes for bare TMF. The small θ value of 1.92 mrad in the fabricated adiabatic TMF prevents the fundamental mode from being excited and maintains its power density within the optical fiber structure. In this scenario, the majority of the light is confined within the fiber core/cladding area, assuming the large refractive index difference between silica core (n_1 = 1.45) and air (n_2 = 1.00). By considering the simple calculation of Snell's Law, $n_1 \sin \theta_1 = n_2 \sin \theta_2$, the calculated critical angle (θ_c) of bare TMF was 43.59°. After the nanocomposite deposition, the transmission of TiO_2-SiO_2-SA reduced to 57–60% (within 1555–1565 nm wavelength range), as plotted in Fig. 6(b). In this case, the nanocomposite served as a new cladding medium with n_2 = 1.3997, consequently reduced the refractive index difference between two media. As per calculation, the θ_c increased to 74.81° after TiO_2-SiO_2-PDMS was spin-coated onto the TMF. Therefore, a fraction of light in the form of evanescent waves that propagate with incidence angle smaller than θ_c will experience dynamic absorption with the embedded TiO_2-SiO_2. Meanwhile, the light with incidence angle larger than θ_c will be internally reflected and remained in the core/cladding region. It is worthy to emphasize that the polymer used in this experiment only served as a medium to secure the nanomaterial, assisted back-coupling of light after the nonlinear interaction and has no contribution towards the saturable absorption effect, as reported in [45].

The TiO_2-SiO_2-SA was inserted into a two-arm experimental setup in Fig. 6(c) for nonlinear measurement. The characteristics of pulse fiber laser source are 150 fs, 60 MHz and 1.56 μm for pulse duration, repetition rate, and central wavelength, respectively. The power adjustment was done by variable optical attenuator (VOA). The power was split equally via optical coupler (OC) and directed to a pair of optical power meters (OPM1 and OPM2) for data collection. The fabricated TiO_2-SiO_2-SA was inserted within one port of OC and OPM2 while the other port (OPM1) was referred as reference power. The nonlinear saturable absorption of TiO_2-SiO_2-SA can be
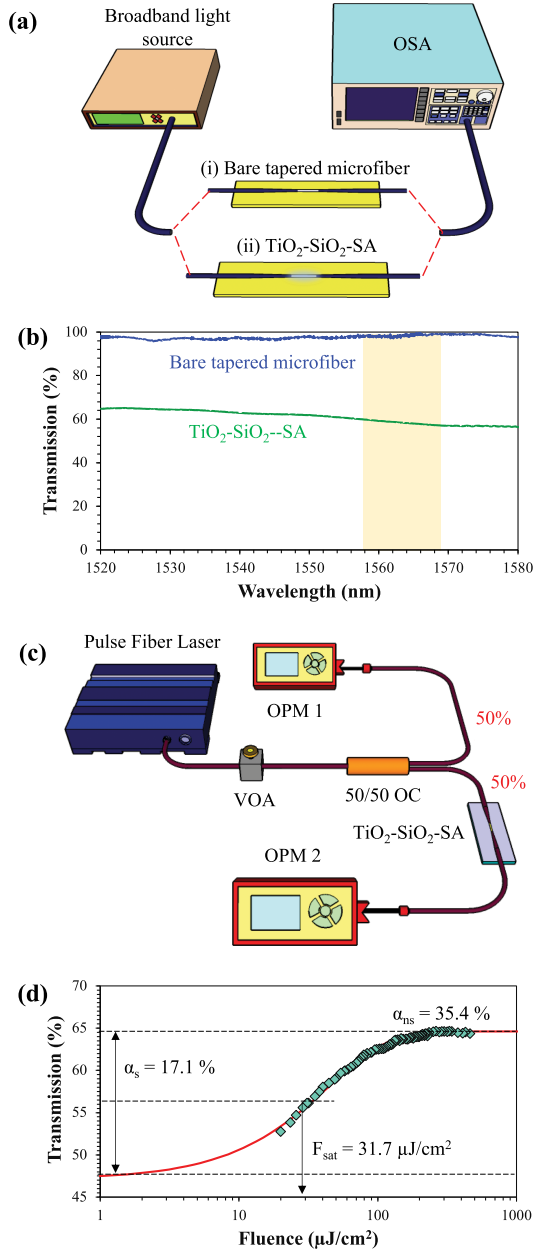
(a)

(b)

(c)

(d)

Fig. 6. Linear transmission measurement (a) experimental setup and (b) transmission profile bare TMF and TiO$_2$-SiO$_2$-SA; nonlinear transmission measurement (c) experimental setup and (d) nonlinear transmission curve of TiO$_2$-SiO$_2$-SA.

understood by three main parameters, specifically modulation depth (α_s), saturation fluence (F_{sat}) and non-saturable loss (α_{ns}), as effectively described in (4) below [46];

$$T(F) = 1 - \alpha_s \cdot e^{\left(\frac{-F}{F_{sat}}\right)} - \alpha_{ns}, \tag{4}$$

where T is the transmittance, and F is the incident fluence. From (4), α_s is estimated from the difference of maximum and minimum transmission, F_{sat} is defined as the incident fluence required to achieve half of α_s. In contrast, α_{ns} is referred to
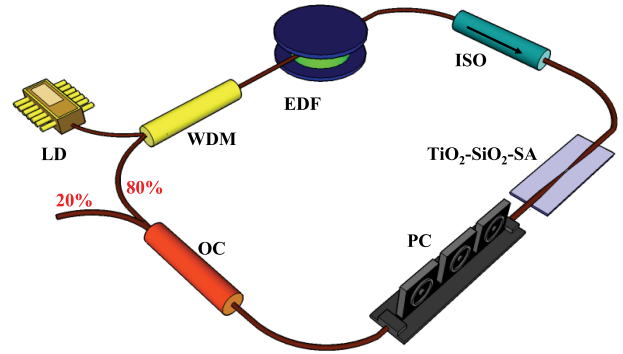

Fig. 7. Experimental setup of the ring cavity ML-EDFL using TiO$_2$-SiO$_2$-SA.

the constant linear loss of TiO$_2$-SiO$_2$-SA. The experimental data and curve fitting of (4) are depicted in Fig. 6(d). From the analysis, α_s, α_{ns} and F_{sat} are determined as 17.1%, 35.4%, and 31.7 μJ/cm^2 (equivalent to I_{sat} of 211 MW/cm^2), respectively. The SA with large modulation depth is able to generate ultrashort pulses as well as suppress multiple pulses including harmonic mode-locking. Therefore, this proves the capability of TiO$_2$-SiO$_2$-SA to allow high fluence of photons to be transmitted and opaque for low fluence of photons, which is the main criterion that must be taken into account for a material to become SA, as mentioned in [47].

III. ERBIUM-DOPED FIBER LASER WITH TIO$_2$-SIO$_2$-SA

A. Experimental Layout

Fig. 7 depicts the experimental layout of ML-EDFL incorporating TiO$_2$-SiO$_2$-SA. The ML-EDFL was ignited by a 980 nm laser diode (LD) with 208 mW maximum pump power. For the active gain medium, 5 m length of erbium-doped fiber (EDF, Lucent HP980) was utilized. The EDF features dispersion coefficient of -18 ps/(nm.km) at 1550 nm and absorption coefficients in the range of 3.5–5.5 dB/m within 1530–1560 nm wavelengths. The pump light was directed into the EDF through a 980/1550 nm wavelength division multiplexing fused coupler (WDM). In order to prevent unwanted back reflections and ensure unidirectional operation, a polarization-independent isolator (ISO) was included right after the EDF. Then, the fabricated TiO$_2$-SiO$_2$-SA was inserted after the ISO as a mode-locker device in the cavity. A three-paddle all-fiber polarization controller (PC) was spliced with the TiO$_2$-SiO$_2$-SA to control the cavity birefringence and optimize its polarization state. An OC with splitting ratio of 80/20 was employed to split the intra-cavity lasing light into two paths; the more significant portion was channelled back into the laser cavity while the smaller portion was tapped out for pulse measurement.

The spectral dynamics of the ML-EDFL were recorded by the optical spectrum analyzer (Yokogawa, AQ6370B) with 0.02 nm resolution bandwidth. The pulse profile was measured with a 100 MHz digital phosphor oscilloscope (Tektronix, TDS 3012C) via 5 GHz bandwidth photodetector (Thorlabs InGaAs detector, DET08CFC). The radio frequency (RF) spectrum was obtained by an electrical spectrum analyzer (GW Instek GSP) with radio

TABLE I
CALCULATION OF GVD IN THE RING CAVITY ML-EDFL

Fiber type	L (m)	β_2 (ps²/km)	Total GVD (ps²)
Hi-1060	1.6	–7	–0.0112
HP-980 EDF	5.0	23	0.1150
SMF-28	13.3	–22	–0.2929
		Net GVD	–0.1891

and video resolution bandwidth (RBW and VBW) of 3 kHz and 1 kHz, respectively. The average output power was measured using OPM (Thorlabs, PM100D) with S302C thermal sensor from 20% of the OC output port. The autocorrelation trace of the ML-EDFL was captured using autocorrelator (A.P.E. PulseCheck). The operating regime of the ML-EDFL was determined by calculating the total group velocity dispersion (GVD) of each fiber used in the laser cavity. The product of each fiber length (L) and its dispersion coefficient (β_2) in Table I confirmed the anomalous dispersion regime of the proposed laser system with the net GVD of -0.1891 ps².

B. Pulse Performance and Stability Evaluation

Fig. 8(a)–(d) depict the spectral evolution of ML-EDFL with respect to pump powers. In the experiment, a continuous wave (CW) laser was initiated when the pump power reached 10.3 mW. By launching the pump power over 72.4 mW, the mode-locking pulses were generated as a result of constructive interference of longitudinal modes after multiple cavity roundtrips. As a result, the typical feature of a soliton pulse with the existence of Kelly sidebands was also observed as shown in Fig. 8(a), (b), arose from the resonance effect between soliton and dispersive wave components after periodic soliton perturbations. These sidebands on the spectral envelopes are an indicator that the proposed ML-EDFL operates in the net negative dispersion which matched with the calculation in Table I. Fig. 8(b) portrays the output spectrum at the threshold and maximum pump powers. For 208 mW pump power, the central wavelength (λ_c) and its 3-dB spectral bandwidth ($\Delta\lambda$) of the ML-EDFL were 1560.13 nm and 4.17 nm, respectively. From these results, there are no significant difference between these optical spectra. However, further analysis can be made to determine the quality of generated pulse from the laser cavity.

Based on the collected data in Fig. 8(a), the analyses of optical spectra in relation to pump powers are plotted in Fig. 8(c). Numerical simulation in [48] stated that the laser cavity with small net anomalous dispersion (GVD > -1 ps²) permits small coefficient of energy transfer from soliton to Kelly sidebands, thus the appearance of weak sidebands in the optical spectrum is commonly observed as shown in Fig. 8(b). The enhancement of peak power intensity for both soliton central wavelength and sidebands were also observed at increasing supplied pump powers, as depicted in Fig. 8(b).

The plots in Fig. 8(c) reveal the evolvement of power difference between soliton's central wavelength and highest Kelly sideband (ΔP), and power difference between sidebands ($\Delta P_{\pm 1}$) from 5.31 to 6.09 dB and 2.17 to 2.87 dB, respectively. The
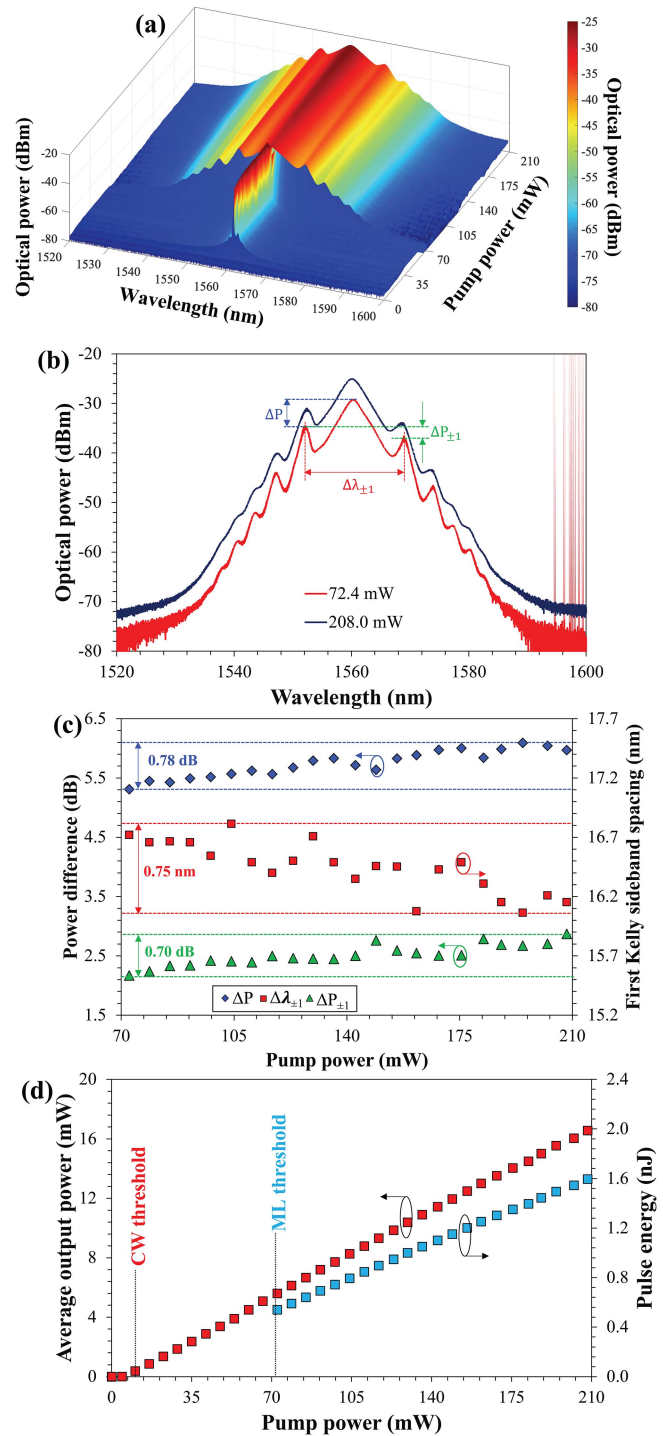
Fig. 8. (a) Spectral evolution, (b) optical spectrum of ML-EDFL using TiO₂-SiO₂-SA at 72.4 mW and 208 mW pump power, (c) analyses of first Kelly sideband, and (d) power and pulse energy development.

maximum difference for both ΔP and $\Delta P_{\pm 1}$ were less than 1 dB, which are considerably small, suggesting the pulse energy concentrated in the soliton pulse rather than Kelly sidebands [48]. This kind of soliton pulse might not be suitable for specific applications like terahertz signal generation where strong sidebands are preferred, yet employing highly nonlinear fiber can significantly enhance those sidebands [48]. However,

the presence of normal dispersion fiber (EDF, in this case) in the laser cavity weakens the Kelly sidebands. This observation is contradicted to the one reported in [49] whereby the Kelly sidebands are dominant in a laser cavity made by all anomalous dispersion fibers. Such resonant interactions between soliton pulses and dispersive waves might restrict the soliton amplification efficiency and induce pulse timing jitter, which degrade pulse's stability and create substantial bit errors over long-distance propagation [49]. To tackle these issues, several strategies have been practiced, such as designing laser resonator with length that is longer than the soliton period, or incorporating optical filter with appropriate bandwidth, namely Lyot filter [49], non-adiabatic tapered fiber [50], and chirped fiber Bragg grating [51]. The purpose of these methods is to reduce the strength of Kelly sidebands. Besides that, assuming fixed cavity dispersion, the spacing between first Kelly sideband ($\Delta\lambda_{\pm 1}$) has inverse relation to the pulse width [52]. Nearly consistent pulse width against pump powers were observed, which is in-line with the minimal decrement of $\Delta\lambda_{\pm 1}$ from 16.81 to 16.06 nm (0.75 nm maximum difference only).

Fig. 8(d) shows the power and pulse energy development against pump powers. The linear increase in the average output power from 5.61 to 16.57 mW was observed with increasing the pump power to its maximum. Based on the findings, the calculated laser efficiency was 7.96%. This corresponded to the pulse energy incremental from 0.54 to 1.59 nJ. By considering the measured output power, the loss of the optical components and SA device in Fig. 7, the maximum intensity injected into TiO₂-SiO₂-SA was estimated to be 24.82 GW/cm², which was determined by back-calculation method. Neither physical damage nor deterioration of pulse performance were observed for the entire experiments, thus the damage threshold of this SA was believed to be larger than this value.

Fig. 9(a) captures the ML-EDFL pulse train at 208 mW pump power. The time interval between subsequent pulses was 96.27 ns that reflected to 10.39 MHz repetition rate, which is in line with 19.9 m cavity length. The RF spectrum in Fig. 9(b) shows the frequency of the ML-EDFL over 500 MHz span, with 65.6 dB signal-to-noise ratio at fundamental frequency. At the highest pump power, no CW component breakthrough or multiple pulsing was observed, highlighting that the optical pulses was in stable condition.

Fig. 10 portrays the autocorrelation trace of ML-EDFL with FWHM of 1.23 ps. The data is fitted with secant hyperbolic (sech²) profile with decorrelation factor of 0.648, giving an estimated pulse width (τ_{pulse}) of 797 fs. The time-bandwidth product (TBP) of the soliton pulse is calculated by using (5) as follows:

$$TBP = \frac{\tau_{pulse} \cdot \Delta\lambda \cdot c}{(\lambda_c)^2} \tag{5}$$

where c is the speed of light in vacuum. From the experimental findings, the calculated TBP of the pulse is 0.41, showing that the pulse was slightly chirped since the theoretical transform limit value is 0.315. A stability test was executed at laboratory environment (>70% relative humidity) for 60 minutes at 208 mW pump power to authenticate the ML-EDFL robustness. The
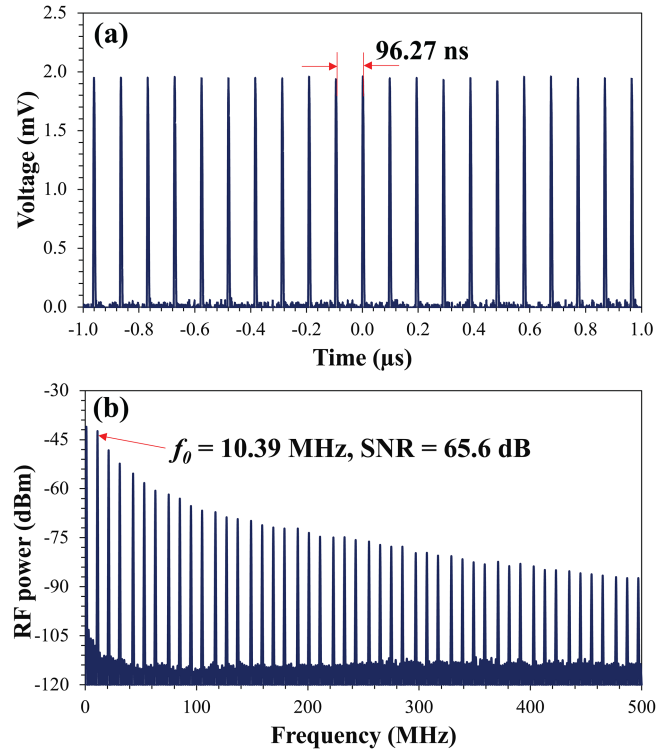
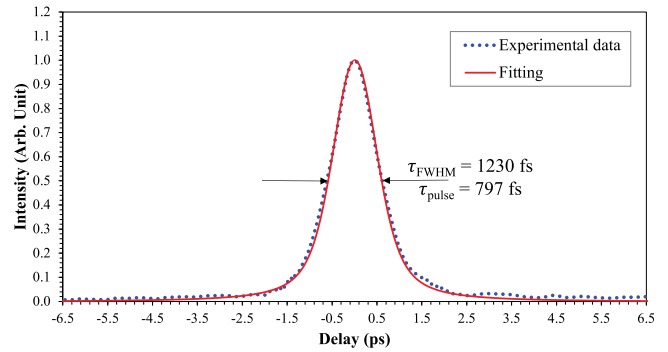Fig. 9. (a) The pulse train and (b) RF spectrum of the ML-EDFL using TiO₂-SiO₂-SA.

Fig. 10. Autocorrelation trace of ML-EDFL using TiO₂-SiO₂-SA.

data collection was performed within 2 minutes interval. The spectrogram of the ML-EDFL optical spectrum and autocorrelation trace over a 60 minutes monitoring period are shown in Fig. 11(a) and (b), respectively. Fig. 11(c) and (d) show the output data in terms of λ_c and $\Delta\lambda$, as well as τ_{pulse} and TBP, in which the plotted error bars were generated from three different measurements with time interval of 10 days. From the analysis, the average λ_c, $\Delta\lambda$, τ_{pulse} and TBP are 1560.07 ± 0.03 nm, 4.01 ± 0.16 nm, 797 ± 7 fs and 0.39 ± 0.02, respectively. This quasi-long-term stability assessment shows the viability of TiO₂-SiO₂-SA based TMF as a reliable nonlinear device for ultrashort pulse generation in near-infrared wavelength bands.
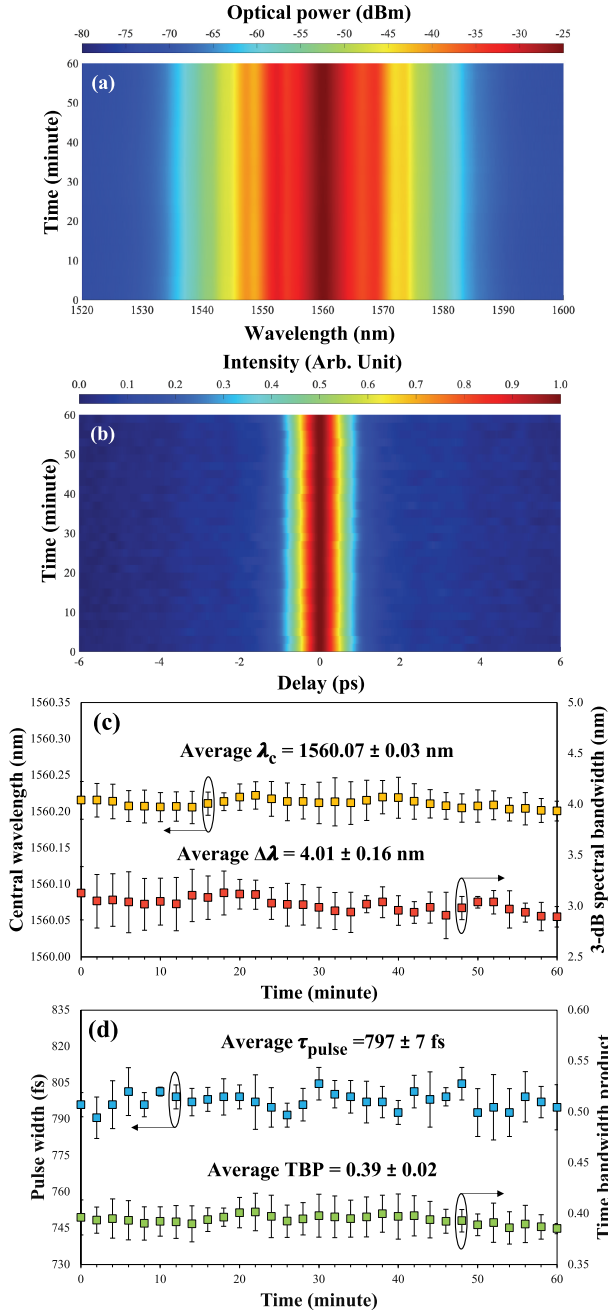
Fig. 11. (a) OSA spectrum, (b) autocorrelation trace, analysis of (c) central wavelength and 3-dB spectral bandwidth; and (d) pulse duration and TBP over 60 min monitoring period.

TABLE II
REVIEWS ON SA PREPARATION METHODS AND THEIR NONLINEAR PROPERTIES

SA	SA preparation	T_{ns} (%)	MD (%)	I_{sat}	Ref.
TiS$_2$/PVA	Spin-coating of polymer composite	17.00	13.19	17.97 MW/cm^2	[53]
Ti$_3$AlC$_2$	Drop and dry	50.80	2.00	2.68 MW/cm^2	[54]
rGO-TiO$_2$	Drop and dry	73.21	32.54	0.42 kW/cm^2	[55]
TiS$_2$	Optical deposition	-	8.30	1.20 mW	[56]
TiO$_2$	Fiber drawing	63.10	-	-	[19]
TiO$_2$-SiO$_2$/PDMS	Spin-coating of polymer composite	35.40	17.10	211.00 MW/cm^2	This work

TABLE III
CRITICAL REVIEWS ON THE PULSE PERFORMANCE OF TI-BASED SAS IN 1.56 μM REGION

Material	ML$_{th}$ (mW)	Pulse width (s)	Rep. Rate (MHz)	P$_{out}$ (mW)	Pulse energy (J)	Ref.
TiS$_2$/PVA	276.0	2.36 p	3.43	0.18	0.05 n	[53]
Ti$_3$AlC$_2$	21.0	2.21 p	1.89	15.30	8.14 n	[54]
rGO-TiO$_2$	100.8	1.05 p	11.18	1.51	0.13 n	[55]
TiS$_2$	-	812.00 f	22.70	0.57	25.3 p	[56]
TiO$_2$	106.0	9.74 p	0.98	8.42	8.56 n	[19]
TiO$_2$-SiO$_2$/ PDMS	72.4	797.00 f	10.39	16.57	1.59 n	This work

*ML$_{th}$: mode-locked threshold power, Rep. rate: repetition rate, P$_{out}$: average output power

IV. DISCUSSION

Table II presents the summary of the SA preparations and non-linear properties of Ti-based SAs. Sandwich of material/polymer composite in between fiber ferrule (FF) is often used to fabricate the SA device, as demonstrated in [53]. The spin-coating method allows controllable thickness of the composite, which correlates to the controllable nonlinear properties of SA [53]. However, the direct light-matter interaction at the FF's core area might lead to the damage of the SA device. In other works, the indirect light coupling method enables a high-power tolerance as compared to the sandwiched thin film in between FFs. Previously, SAs were fabricated by depositing Ti$_3$AlC$_2$ [54] and rGO-TiO$_2$ [55] solutions onto side-polished fibers (SPFs) via simple drop and dry technique. However, the uncontrolled surface roughness caused by polishing effect might contribute to the inhomogeneous surface morphology of the deposited material and enhanced scattering effect, resulting to the high transmission loss of the Ti$_3$AlC$_2$-SA [54] and rGO-TiO$_2$-SA [55]. On the contrary, the work reported by Zhu et al. [56] successfully transferred TiS$_2$ nanosheets onto SPF through an optical deposition method, yielding a lower loss compared to [54], [55]. The optical deposition offers a controllable material attachment onto the substrate, whereby it is highly dependent on the wavelength and power of the pump source, solvent used and deposition time. Other than that, a multimode fiber SA (FSA) contained anatase TiO$_2$ offers a high-power tolerance, yet a pulling tower is required to draw the fiber from a preform [19]. From Table II, the modulation depth of TiO$_2$-SiO$_2$-SA was characterized to be 17.10%, which is higher than [53], [54], [56] and significantly lower than [55].

Table III presents the critical parameters of pulse performance; specifically, threshold condition of mode-locked operation, pulse width, repetition rate, output power and pulse energy. The work in [54] exhibited low mode-locking threshold condition of 21.0 mW due to the low saturation intensity of Ti$_3$AlC$_2$-SA. Although rGO-TiO$_2$ [55] possessed lower saturation intensity, a higher pump power is required to compensate the high insertion loss of the SA device, thus mode-locking operation was observed at 100.8 mW. Despite of the highest saturation intensity attained in this work as compared to others [53], [54], [55], [56], it is worth to mention that with the

optimized laser cavity in this experiment, the mode-locking operation started at 72.4 mW, which is relatively lower than [19], [53], [55] and significantly higher than [54]. Besides that, the pulse width in the works [19], [53], [54], [55] lies within picosecond duration, while Zhu et al. [56] reported ultrafast duration of 812 fs via TiS_2-SA, which is slightly slower than this work (797 fs). Despite of large power extraction and short cavity length, the output power attained by Zhu et al. [56] was less than 1 mW with picojoules pulse energy. Contrarily, when the long length of laser cavity is designed, it allows the accumulation of the intracavity pulse energy yet sacrificing its pulse width [19], [54]. Therefore, based on the abovementioned works, this work delivered the output power of 16.57 mW, which is higher output power and fastest pulse duration within TiO_2 group and clearly better than other Ti-based SAs [19], [53], [54], [55], [56].

The reduced diameter of the optical fiber to 10 μm allows light-matter interaction within the evanescent field which consequently creates the intensity dependent saturable absorption effect. Furthermore, the incorporation of SiO_2 as a coating layer helps to protect the TiO_2 nanoparticles from any chemical degradation as well as minimizes their aggregation. Additionally, the water-insoluble polymer like PDMS acts as a second protective barrier to ensure oxygen and moisture free environment and prolong the shelf life of the device. Moreover, the involvement of low refractive index polymer in this experiment secures the back-reflection of light following nonlinear interaction at the thin waist of TMF. Neither pulse instabilities nor thermal damage of the SA device was observed for the entire experiment. The threshold damage of the fabricated TiO_2-SiO_2-SA was beyond 24.82 GW/cm² thus opens new possibilities for future advances in nonlinear photonic devices.

V. CONCLUSION

We experimentally demonstrated the potential of TiO_2-SiO_2-PDMS nanocomposite as a new nanomaterial for femtosecond pulse generation at 1.56 μm wavelength. The ML-EDFL was initiated at 72.4 mW pump power and remained as a fundamental pulse at 10.39 MHz of repetition rate. The shortest pulse duration achieved was 797 fs, which is a significant improvement among the TiO_2 families and other Ti-based SAs albeit using waste as a starting material. Pulse-breaking effect was successfully suppressed due to the high modulation depth of 17.1%. The incorporation of SiO_2 layer preserved the material from chemical degradation and minimizing the photo-ablation of material. Thus, the TiO_2-SiO_2-SA is believed to sustain at large light intensity of at least 24.82 GW/cm². This work explored the potential of TiO_2-SiO_2-SA as future low cost and broadband optical nonlinear device covering up to near-infrared wavelength operation using simple routes of alkali fusion method and spin-coating technique.

REFERENCES

[1] F. Bonaccorso, Z. Sun, T. Hasan, and A. C. Ferrari, "Graphene photonics and optoelectronics," *Nature Photon.*, vol. 4, no. 9, pp. 611–622, 2010.

[2] K. Y. Lau and D. Hou, "Recent research and advances of material-based saturable absorber in mode-locked fiber laser," *Opt. Laser Technol.*, vol. 137, 2021, Art. no. 106826.

[3] X. Liu, Q. Gao, Y. Zheng, D. Mao, and J. Zhao, "Recent progress of pulsed fiber lasers based on transition-metal dichalcogenides and black phosphorus saturable absorbers," *Nanophotonics*, vol. 9, no. 8, pp. 2215–2231, 2020.

[4] N. Z. A. Naharuddin et al., "Pulsed-laser-ablated gold-nanoparticles saturable absorber for mode-locked erbium-doped fiber lasers," *Opt. Laser Technol.*, vol. 150, 2022, Art. no. 107875.

[5] A. R. Muhammad, M. T. Ahmad, R. Zakaria, P. P. Yupapin, S. W. Harun, and M. Yasin, "Mode-locked thulium doped fibre laser with copper thin film saturable absorber," *J. Modern Opt.*, vol. 66, no. 13, pp. 1381–1385, 2019.

[6] W. A. Khaleel, S. A. Sadeq, I. A. M. Alani, and M. H. M. Ahmed, "Magnesium oxide (MgO) thin film as saturable absorber for passively mode locked erbium-doped fiber laser," *Opt. Laser Technol.*, vol. 115, pp. 331–336, 2019.

[7] S. A. Sadeq, S. W. Harun, and A. H. Al-Janabi, "Ultrashort pulse generation with an erbium-doped fiber laser ring cavity based on a copper oxide saturable absorber," *Appl. Opt.*, vol. 57, pp. 5180–5185, 2018.

[8] M. A. W. A. Hadi et al., "Investigation of tungsten trioxide as a saturable absorber for mode-locked generation," *Opt. Laser Technol.*, vol. 132, 2020, Art. no. 106496.

[9] J. S. Liu et al., "Fe_3O_4 nanoparticles as a saturable absorber for giant chirped pulse generation," *Beilstein J. Nanotechnol.*, vol. 10, no. 1, pp. 1065–1072, 2019.

[10] A. Soussi et al., "Electronic and optical properties of TiO_2 thin films: Combined experimental and theoretical study," *J. Electron. Mater.*, vol. 50, no. 8, pp. 4497–4510, 2021.

[11] L. Cui and W. Wang, "Optical properties of anatase and rutile TiO_2 films deposited by using a pulsed laser," *Appl. Opt.*, vol. 60, no. 27, pp. 8453–8457, 2021.

[12] G. Li, M. Fu, Y. Zheng, and X. Guan, "TiO_2 microring resonators with high Q and compact footprint fabricated by a bottom-up method," *Opt. Lett.*, vol. 45, no. 18, pp. 5012–5015, 2020.

[13] A. Mammeri et al., "Optogeometric study of multimode TiO_2 waveguide thin films elaborated by reactive magnetron sputtering," *Physica B: Condens. Matter*, vol. 641, 2022, Art. no. 414059.

[14] K. Hammani et al., "Octave spanning supercontinuum in titanium dioxide waveguides," *Appl. Sci.*, vol. 8, no. 4, 2018, Art. no. 543.

[15] A. Kumar, P. Choudhary, A. Kumar, P. H. C. Camargo, and V. Krishnan, "Recent advances in plasmonic photocatalysis based on TiO_2 and noble metal nanoparticles for energy conversion, environmental remediation, and organic synthesis," *Small*, vol. 18, no. 1, 2022, Art. no. 2101638.

[16] C. Zhou, Z. Xi, D. J. Stacchiola, and M. Liu, "Application of ultrathin TiO_2 layers in solar energy conversion devices," *Energy Sci. Eng.*, vol. 10, no. 5, pp. 1614–1629, 2022.

[17] M. H. M. Ahmed et al., "Nanosized titanium dioxide saturable absorber for soliton mode-locked thulium-doped fiber laser," *Results Phys.*, vol. 31, 2021, Art. no. 104930.

[18] H. Ahmad et al., "C-band Q-switched fiber laser using titanium dioxide (TiO_2) as saturable absorber," *IEEE Photon. J.*, vol. 8, no. 1, 2015, Art. no. 1500107.

[19] P. H. Reddy et al., "Titanium dioxide doped fiber as a new saturable absorber for generating mode-locked erbium doped fiber laser," *Optik*, vol. 158, pp. 1327–1333, 2018.

[20] M. F. M. Rusdi et al., "Titanium dioxide (TiO_2) film as a new saturable absorber for generating mode-locked thulium-holmium doped all-fiber laser," *Opt. Laser Technol.*, vol. 89, pp. 16–20, 2017.

[21] B. Gao et al., "Ta_4C_3 MXene as a saturable absorber for femtosecond mode-locked fiber lasers," *J. Alloys Compd.*, vol. 900, 2022, Art. no. 163529.

[22] B. Guo et al., "Sub-200 fs soliton mode-locked fiber laser based on bismuthene saturable absorber," *Opt. Exp.*, vol. 26, no. 18, pp. 22750–22760, 2018.

[23] D. Na, K. Park, K. Park, and Y. Song, "Passivation of black phosphorus saturable absorbers for reliable pulse formation of fiber lasers," *Nanotechnol.*, vol. 28, no. 47, 2017, Art. no. 475207.

[24] A. A. Kashale et al., "Biomediated green synthesis of TiO_2 nanoparticles for lithium ion battery application," *Composites Part B. Eng.*, vol. 99, pp. 297–304, 2016.

[25] M. Cargnello, T. R. Gordon, and C. B. Murray, "Solution-phase synthesis of titanium dioxide nanoparticles and nanocrystals," *Chem. Rev.*, vol. 114, no. 19, pp. 9319–9345, 2014.

[26] S. Mallakpour and M. Naghdi, "Polymer/SiO$_2$ nanocomposites: Production and applications," *Prog. Mater. Sci.*, vol. 97, pp. 409–447, 2018.

[27] M. C. Le et al., "Synthesizing and evaluating the photocatalytic and antibacterial ability of TiO$_2$/SiO$_2$ nanocomposite for silicate coating," *Fron. Chem.*, vol. 9, 2021, Art. no. 738969.

[28] B. Xu et al., "Hydrogen sensor based on polymer-filled hollow core fiber with Pt-loaded WO$_3$/SiO$_2$ coating," *Sensors Actuators B Chem.*, vol. 245, pp. 516–523, 2017.

[29] R. Rubab, S. Ali, A. U. Rehman, S. A. Khan, and A. M. Khan, "Templated synthesis of NiO/SiO$_2$ nanocomposite for dye removal applications: Adsorption kinetics and thermodynamic properties," *Colloids Surf. A: Physicochem. Eng. Aspects*, vol. 615, 2021, Art. no. 126253.

[30] V. V. Tyukavkina, E. A. Shchelokova, A. V. Tsyryatyeva, and A. G. Kasikov, "TiO$_2$–SiO$_2$ nanocomposites from technological wastes for self-cleaning cement composition," *J. Building Eng.*, vol. 44, 2021, Art. no. 102648.

[31] L. Li et al., "Mode-locked Er-doped fiber laser by using MoS$_2$/SiO$_2$ saturable absorber," *Nanoscale Res. Lett.*, vol. 14, no. 1, pp. 1–7, 2019.

[32] S. Liu et al., "Passively mode-locked fiber laser with WS$_2$/SiO$_2$ saturable absorber fabricated by sol–gel technique," *ACS Appl. Mater. Interfaces*, vol. 12, no. 26, pp. 29625–29630, 2020.

[33] R. Lv et al., "Optical properties and applications of molybdenum disulfide/SiO$_2$ saturable absorber fabricated by sol-gel technique," *Opt. Exp.*, vol. 27, no. 5, pp. 6348–6356, 2019.

[34] Z. Chen et al., "Improved optical damage threshold graphene oxide/SiO$_2$ absorber fabricated by sol-gel technique for mode-locked erbium-doped fiber lasers," *Carbon*, vol. 144, pp. 737–744, 2019.

[35] N. S. Rosli, C. A. C. Abdullah, and R. Hazan, "Synthesis, characterization and investigation of photocatalytic activity of nano-titania from natural ilmenite with graphite for cigarette smoke degradation," *Results Phys.*, vol. 11, pp. 72–78, 2018.

[36] E. M. Mahdi, M. Hamdi, M. S. M. Yusoff, and P. Wilfred, "XRD and EDXRF analysis of anatase nano-TiO$_2$ synthesized from mineral precursors," *Adv. Mat. Res.*, vol. 620, pp. 179–185, 2013.

[37] T. Theivasanthi and M. Alagar, "Titanium dioxide (TiO$_2$) nanoparticles XRD analyses: An insight," Jul. 2013, *arxiv.org/abs/1307.1091*.

[38] T. T. H. Tran, H. Kosslick, A. Schulz, and Q. L. Nguyen, "Photocatalytic performance of crystalline titania polymorphs in the degradation of hazardous pharmaceuticals and dyes," *Adv. Natural Sci. : Nanosci. Nanotechnol.*, vol. 8, no. 1, 2017, Art. no. 15011.

[39] A. Jaroenworaluck, N. Pijarn, N. Kosachan, and R. Stevens, "Nanocomposite TiO$_2$-SiO$_2$ gel for UV absorption," *Chem. Eng. J.*, vol. 181, pp. 44–55, 2012.

[40] M. B. John, S. W. Mugo, and J. M. Ngaruiya, "Dependence of optical band gap on crystallite size of TiO$_2$ thin films prepared using sol gel process," *Eur. J. Mater. Sci.*, vol. 8, no. 1, pp. 1–12, 2021.

[41] R. I. Woodward and E. J. R. Kelleher, "2D saturable absorbers for fibre lasers," *Appl. Sci.*, vol. 5, no. 4, pp. 1440–1456, 2015.

[42] S. Ravets et al., "Intermodal energy transfer in a tapered optical fiber: Optimizing transmission," *J. Opt. Soc. Amer. A*, vol. 30, no. 11, pp. 2361–2371, 2013.

[43] A. Wypych et al., "Dielectric properties and characterisation of titanium dioxide obtained by different chemistry methods," *J. Nanomater.*, vol. 2014, 2014, Art. no. 124814.

[44] F. M. Sánchez-Arévalo et al., "Photomechanical response of composites based on PDMS and carbon soot nanoparticles under IR laser irradiation," *Opt. Mater. Exp.*, vol. 5, no. 8, pp. 1792–1805, 2015.

[45] N. M. Yusoff et al., "Molybdenum trioxide decorated on tapered microfiber for mode-locked erbium-doped fiber laser," *J. Mater. Res. Technol.*, vol. 14, pp. 942–953, 2021.

[46] M. E. Fermann, A. Galvanauskas, and G. Sucha, *Ultrafast Lasers: Technology and Applications*. Boca Raton, FL, USA: CRC Press, 2002, vol. 80.

[47] S. A. Hussain, "Discovery of several new families of saturable absorbers for ultrashort pulsed laser systems," *Sci. Rep.*, vol. 9, no. 1, pp. 1–9, 2019.

[48] W. Zhao, C. Yang, and M. Shen, "Enhanced Kelly sidebands of mode-locking fiber lasers for efficient terahertz signal generation," *Opt. Laser Technol.*, vol. 137, 2021, Art. no. 106802.

[49] J. Li et al., "Kelly sideband suppression and wavelength tuning of a conventional soliton in a Tm-doped hybrid mode-locked fiber laser with an all-fiber Lyot filter," *Photon. Res.*, vol. 7, no. 2, pp. 103–109, 2019.

[50] Y. Wang et al., "Tunable and switchable dual-wavelength mode-locked Tm^{3+}-doped fiber laser based on a fiber taper," *Opt. Exp.*, vol. 24, no. 14, pp. 15299–15306, 2016.

[51] X. Liu et al., "Versatile multi-wavelength ultrafast fiber laser mode-locked by carbon nanotubes," *Sci. Rep.*, vol. 3, no. 1, pp. 1–6, 2013.

[52] Y. H. Lin and G. R. Lin, "Kelly sideband variation and self four-wave-mixing in femtosecond fiber soliton laser mode-locked by multiple exfoliated graphite nano-particles," *Laser Phys. Lett.*, vol. 10, no. 4, 2013, Art. no. 45109.

[53] X. Shang, L. Guo, H. Zhang, D. Li, and Q. Yue, "Titanium disulfide based saturable absorber for generating passively mode-locked and Q-switched ultra-fast fiber lasers," *Nanomater.*, vol. 10, no. 10, 2020, Art. no. 1922.

[54] A. A. A. Jafry et al., "Soliton mode-locked pulse generation with a bulk structured MXene Ti$_3$AlC$_2$ deposited onto a D-shaped fiber," *Appl. Opt.*, vol. 59, no. 28, pp. 8759–8767, 2020.

[55] H. Ahmad, S. A. Reduan, N. Yusoff, M. F. Ismail, and S. N. Aidit, "Mode-locked pulse generation in erbium-doped fiber laser by evanescent field interaction with reduced graphene oxide-titanium dioxide nanohybrid," *Opt. Laser Technol.*, vol. 118, pp. 93–101, 2019.

[56] X. Zhu et al., "TiS$_2$-based saturable absorber for ultrafast fiber lasers," *Photon. Res.*, vol. 6, no. 10, pp. C44–C48, 2018.